2020

Microstructural evolution of nanotwinned Al-Zr alloy with significant 9R phase

N.A. Richter

Y.F. Zhang

D. Y. Xie

R. Su

Q. Li

See next page for additional authors

Authors

N.A. Richter, Y.F. Zhang, D. Y. Xie, R. Su, Q. Li, S. Xue, T. Niu, J. Wang, H. Wang, and Xinghang Zhang

MATER. RES. LETT.
2020, VOL. 9, NO. 2, 91–98
https://doi.org/10.1080/21663831.2020.1840451

MATERIALS RESEARCH LETTERS
Taylor & Francis
Taylor & Francis Group

ORIGINAL REPORT

Microstructural evolution of nanotwinned Al-Zr alloy with significant 9R phase

N. A. Richter [a], Y. F. Zhang [a], D. Y. Xie[b], R. Su [a], Q. Li [a], S. Xue [a], T. Niu[a], J. Wang [b], H. Wang [a,c] and X. Zhang [a]

[a]School of Materials Engineering, Purdue University, West Lafayette, IN, USA; [b]Mechanical and Materials Engineering, University of Nebraska-Lincoln, Lincoln, NE, USA; [c]School of Electrical and Computer Engineering, Purdue University, West Lafayette, IN, USA

ABSTRACT

Aluminum (Al) alloys have a multitude of applications, notably in the automotive, aerospace and coating industries, yet they exhibit significantly lower mechanical strength than conventional steels. Nanotwins drastically improve mechanical strength while retaining ductility. However, the high SFE of Al largely prevents twinning. Here, we synthesize Al-Zr alloy films containing an abundance of incoherent twin boundaries and 9R phases. These alloys exhibit an extended solid solubility of Zr, retaining a columnar nanotwinned structure across all compositions. These films reach a hardness up to 4.2 GPa with 10 at% Zr and demonstrate the capacity for producing strong Al alloys with nanotwins.

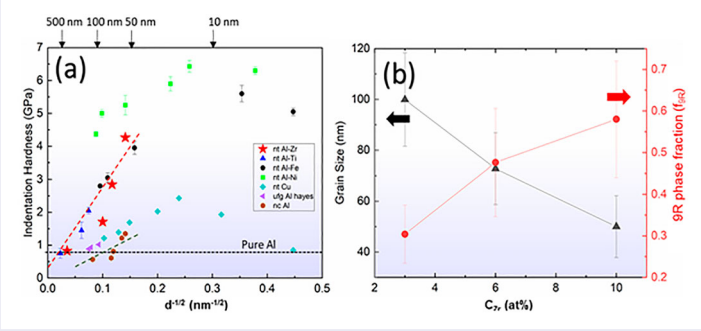

ARTICLE HISTORY
Received 13 August 2020

KEYWORDS
Nanotwinned Al; 9R phase; stacking fault energy; magnetron sputtering

Introduction

The fabrication of high-strength, light-weight components remains crucial for the transportation industry for improving fuel efficiency without sacrificing safety [1]. Wear-resistant Al alloy coatings also have a variety of applications. However, the highest yield strength of commercial Al alloys is ~700 MPa seen in precipitation strengthened 7075 Al alloys [2,3]. Conventional methods for strengthening Al include grain refinement [4,5], precipitation hardening [3], solid solution strengthening [6,7], and work hardening [8], with more recent efforts focusing on severe plastic deformation (SPD) [9] and mechanical alloying [10]. Further improving the mechanical strength of Al alloys to beyond 1 GPa, a level comparable to high strength steels, remains a significant challenge.

Over the past two decades, nanotwinned (NT) metals have garnered significant attention [11]. Many studies have focused on low stacking fault energy (SFE) metals that readily form growth twins, such as Cu (SFE ~ 22 mJ/m^2) [12–14], Ag (SFE ~16 mJ/m^2) [15] and 330 stainless steels (SFE ~40-50 mJ/m^2) [16]. NT metals contain abundant Σ3(111) coherent twin boundaries (CTBs) and Σ3(112) incoherent twin boundaries (ITBs) [11–13,15,17], and NT Cu reached impressive yield strengths without sacrificing tensile ductility [12]. TBs obstruct dislocation motion, similar to grain boundaries, leading to strengthening with a reduction in twin spacing, while ductility is maintained due to TB induced work hardening [18], detwinning and the migration of partial dislocations [13]. Both molecular dynamics (MD) simulations [19,20] and in-situ nanoindentation [21–23]

CONTACT X. Zhang xzhang98@purdue.edu School of Materials Engineering, Purdue University, West Lafayette, IN 47907, USA

Supplemental data for this article can be accessed here. https://doi.org/10.1080/21663831.2020.1840451

have confirmed the high barrier strength of CTBs to the transmission of dislocations.

In contrast, the SFE of Al is significantly larger ($\sim$ 120-160 mJ/m^2) [24] than most FCC metals, meaning a lower propensity for twin formation. Bufford et al. demonstrated the ability of twin replication from a Ag buffer layer into an Al film fabricated by magnetron sputtering [25,26]. The low SFE of the buffer layer, as well as the coherency between the interface buffer layer and the high SFE Al layer, is crucial for this twin formation mechanism [27]. Later, it was revealed that TBs could be introduced into sputtered Al by tailoring the film thickness and texture [28,29]. Recently, various sputtered binary Al-X (X = Fe, Ti, Ni, Co, Mg) alloy systems have been shown to have abundant ITBs [30–36]. These boundaries in Al are strong barriers to dislocation motion, as demonstrated by in-situ nanoindentation [22]. The atomic-scale structure of these ITBs can be described as a periodic vertical array of 3 Shockley partial dislocations, with b_1 being easier to glide than the other two partials under a high applied stress [37,38]. Consequently, ITBs can be mobile under high stresses [38], and a sharp ITB (often containing high stress) can become a diffuse ITB and form 9R phase, a periodic stacking fault structure [37,38]. The 9R phase is important to the maintenance of plasticity in NT Al as shown by both experiments and MD simulation [30,32,33].

Zr is frequently used in cast or wrought Al alloys, however, the influence of Zr solute on the microstructural evolution and TB formation in Al coatings remains unknown. In this work, we show that the addition of Zr solute promotes the formation of a high density of ITBs and a large volume fraction of 9R phase in sputtered Al. The microstructure forms columnar grains with vertically oriented ITBs. Increasing Zr solute composition leads to greater volume fraction of 9R and a high hardness of 4.2 GPa. This study highlights the capability for producing high-strength Al-Zr alloys through the introduction of ITBs and 9R phase.

Materials and methods

Al-Zr films with a Ag seed layer were deposited using magnetron sputtering on HF etched Si(111) substrates. Both out-of-plane $\theta-2\theta$ and pole figure X-ray diffraction (XRD) scans were completed using a Panalytical Empyrean X'pert PRO MRD diffractometer. Transmission electron microscopy (TEM) samples were prepared by mechanical polishing followed by low-energy Ar ion milling. Plan-view and cross-section TEM (XTEM) images were taken using an FEI Talos 200X analytical microscope operated at 200 kV. EDS experiments were performed on the FEI Talos 200X microscope, equipped with a Fischione ultra-high-resolution high angle annular dark field (HAADF) detector and super X energy-dispersive X-ray spectroscopy (EDS) detector. Crystallographic orientation mapping and grain boundary misorientation measurements were made using Nanomegas ASTAR^{TM} with a camera length of 205 mm, a precession angle of 0.5°, and a step size of 5 nm in the same TEM. Hardness and modulus measurements were conducted using nanoindentation with a Hysitron TI Premier nanoindenter.

Results

As shown in Figure 1(a), the Al-Zr films possess strong out-of-plane 111 texture, as labeled on the XRD patterns, and no Al-Zr intermetallic peaks were observed, indicating a solid solution formed at all compositions. The pole figures in Figure 1(b–d) further confirm the strong 111 texture, and the Al-Zr alloys in Figure 1(c,d) exhibit six-fold symmetry, revealing the presence of TBs in the structure. The relative intensity of the twin spots increases with Zr content, providing a qualitative assessment of the twin density within the films. The streaks between spots also identify in-plane rotation of crystals in the Al-10Zr pole figure.

Bright-field (BF) plan-view TEM images in Figure 2(a–c) taken along the $<111>$ zone axis reflect the microstructural evolution. There is a clear structural transition from a single-crystal-like structure possessing uniform texture across the sample and minimal in-plane rotation ($\leq$ 3 at.% Zr), to a nanocrystalline structure with significant in-plane rotation ($\geq$ 6 at.% Zr), as demonstrated by the inserted selected area diffraction (SAD) patterns. Furthermore, the inverse pole figures (IPFs) in Figure 2(d) show uniform $<110>$ in-plane texture in the Al-3Zr sample. A kernel average misorientation (KAM) map (Figure S3) reveals misorientation angles below 5° in the structure, identifying boundary features similar to the features in the BFTEM image in Figure 2(a). Further Zr addition led to columnar grain refinement and significant in-plane rotation, leading to a nanocrystalline structure, reflected in the IPFs in Figure 2(e,f). Figure 2(g) shows the average grain size of Al decreased to 50 nm in the Al-10Zr, whereas pure Al had a large grain size of $\sim$ 450 nm. Meanwhile, the addition of Zr led to significant hardening, from 0.75 GPa for pure Al to 4.2 GPa for the Al-10Zr.

Cross-section TEM (XTEM) images (Figure 3(a,d,g)) taken along the $<110>$ zone axis display columnar grains bounded by Σ3112 ITBs. The twinned structure is confirmed by a second set of spots appearing in the corresponding SAD patterns (labeled in Figure 3(a) SAD

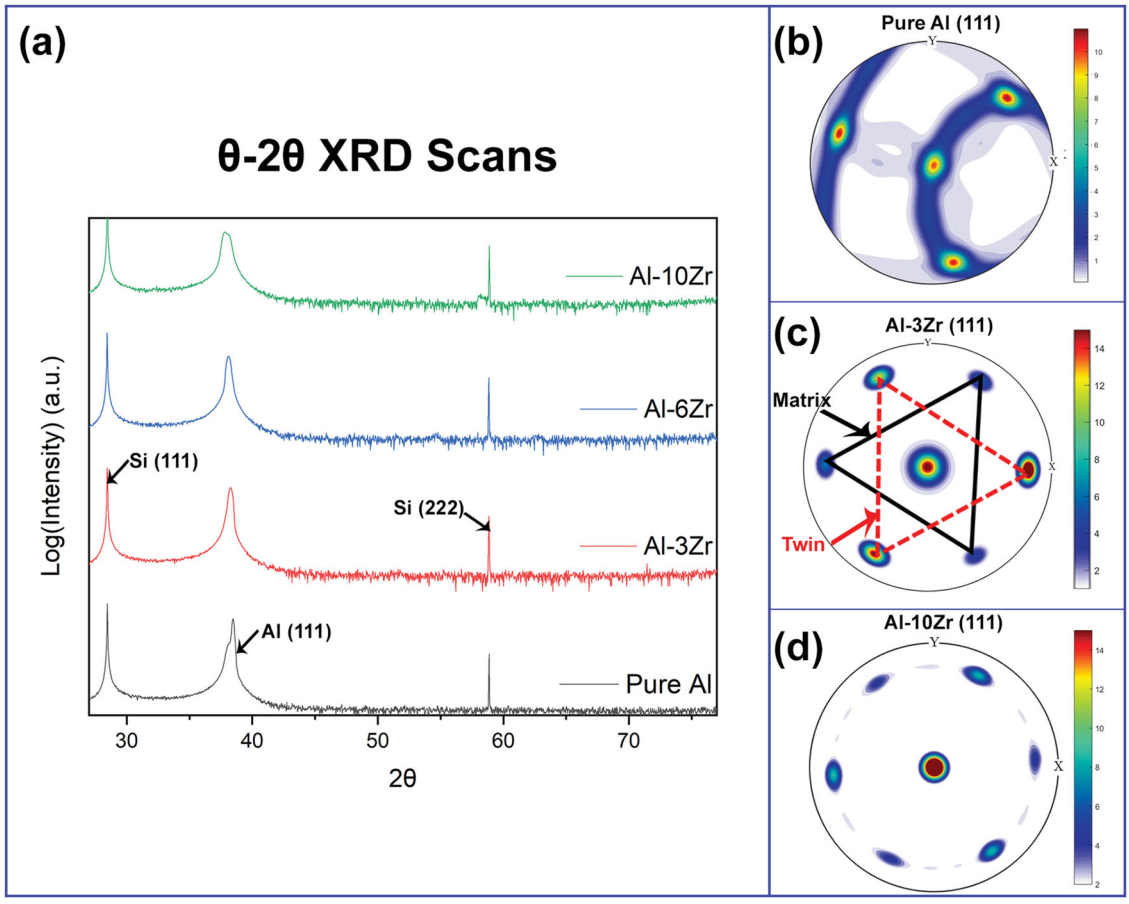

Figure 1. (a) XRD θ-2θ scans of sputtered Al-Zr on Si(111) substrates identifying strong (111) texture. (b-d) XRD (111) pole figure analysis revealing clear six-fold symmetry after introducing Zr, indicating twin variant formation.

inset). The ITB spacing scales inversely with Zr content, leading to clear columnar grain refinement. The additional diffraction spots from the 1/3 111 position reflect the presence of 9R phase. The EDS scans shown in Figure 3(b,e,h) confirm that a complete solid solution forms in all films, even at 10 at.% Zr. This observation underscores the high degree of solubility achieved in the far-from-equilibrium state via the sputtering technique. High-resolution TEM (HRTEM) images uncover a sharp, narrow ITB in Al-3Zr (Figure 3(c)) and broad diffuse ITBs (9R phase) stabilized with higher Zr content (Figure 3(f,i)). The Fast-Fourier Transform (FFT) insets in each HRTEM image indicates the presence of 9R phase. Interestingly, increasing the Zr content leads to broader patches of 9R phase, with some phases expanding across multiple columns (beyond 100 nm).

Figure 4(a) compares the Hall-Petch plot from this study with other NT Al alloys, nanocrystalline (NC) Al alloys, and NT Cu [9,13,30–32,39]. It is evident the hardness of NT Al-Zr increases from 1.7 GPa in the Al-3Zr films to 4.2 GPa in the Al-10Zr films, far beyond the NC Al alloys and NT Cu. The NT Al-Zr alloys also possess a higher Hall-Petch slope ($\sim$9.29 GPa nm$^{1/2}$) than both NC Al and NT Cu. Furthermore, the hardness of NT Al-Zr is comparable to NT Al–Fe [30], but slightly less than NT Al-Ni [32] with similar grain sizes. Figure 4(b) shows that higher levels of Zr lead to the increasing fraction of 9R phase, with nearly 60% of columns containing 9R phase at 10 at.% Zr, one of the highest fractions of 9R phase documented in NT Al alloys.

Discussion

The microstructures of NT Al-Zr undergo an interesting evolution with increasing Zr content, clearly showing both refinement of the twinned grains and an increase in 9R phase. Typically, the high SFE barrier ($\sim$120-160 mJ/m^2) prevents the formation of both twins and 9R phase in Al alloys. The sputtered Al-Zr alloys have strong 111 growth texture, promoted by the single-crystal substrate and the Ag seed layers. Each sample was deposited on top of a 40nm Ag seed layer, which possesses a similar lattice parameter with Al, promoting the strong 111 texture that facilitates the formation of ITBs [25]. Since the Ag seed layer is consistent in all samples, the variation in twin density is clearly attributed to the increasing

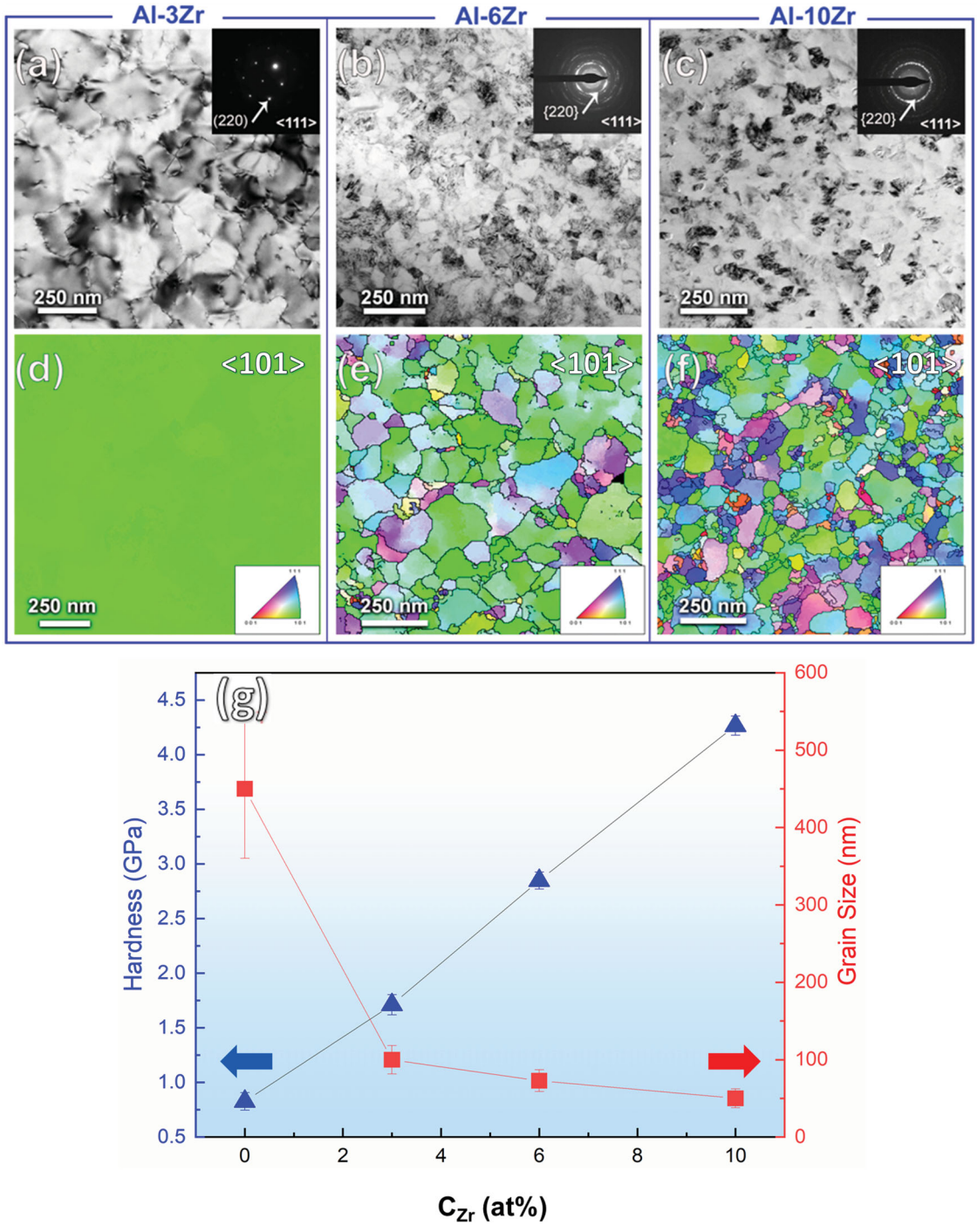

Figure 2. (a–c) Plan-view TEM micrographs with corresponding selected area diffraction (SAD) patterns with increasing Zr content. The microstructure transitions from single-crystal-like (Al-3Zr) to nanocrystalline (Al-6Zr, Al-10Zr). (d–f) In-plane inverse pole figures (IPF) along the $< 101 >$ direction, confirming the single-crystal-like structure in Al-3Zr with consistent in-plane $< 101 >$ texture across the entire sample, and the formation of polycrystalline nanograins and grain refinement upon further Zr additions. (g) Plot depicting grain size (d) and hardness evolution with increasing Zr content.

Zr content. As described by Xue et al., the film growth process leads to the formation of ITBs as two twinned nuclei coalesce and form an ITB to minimize interfacial energy [29]. ITBs consist of a periodic array of Shockley partial dislocations with a b_2:b_1:b_3 arrangement, where b_2 and b_3 are mixed partial dislocations with Burgers vectors of 1/6 $[\bar{2}11]$ and 1/6 $[1\bar{2}1]$, respectively, and b_1 is a pure edge partial dislocation with a Burgers vector of 1/6 $[11\bar{2}]$ [37]. With the glide of the b_1 partial dislocation away from b_2 and b_3, the core energy is reduced and

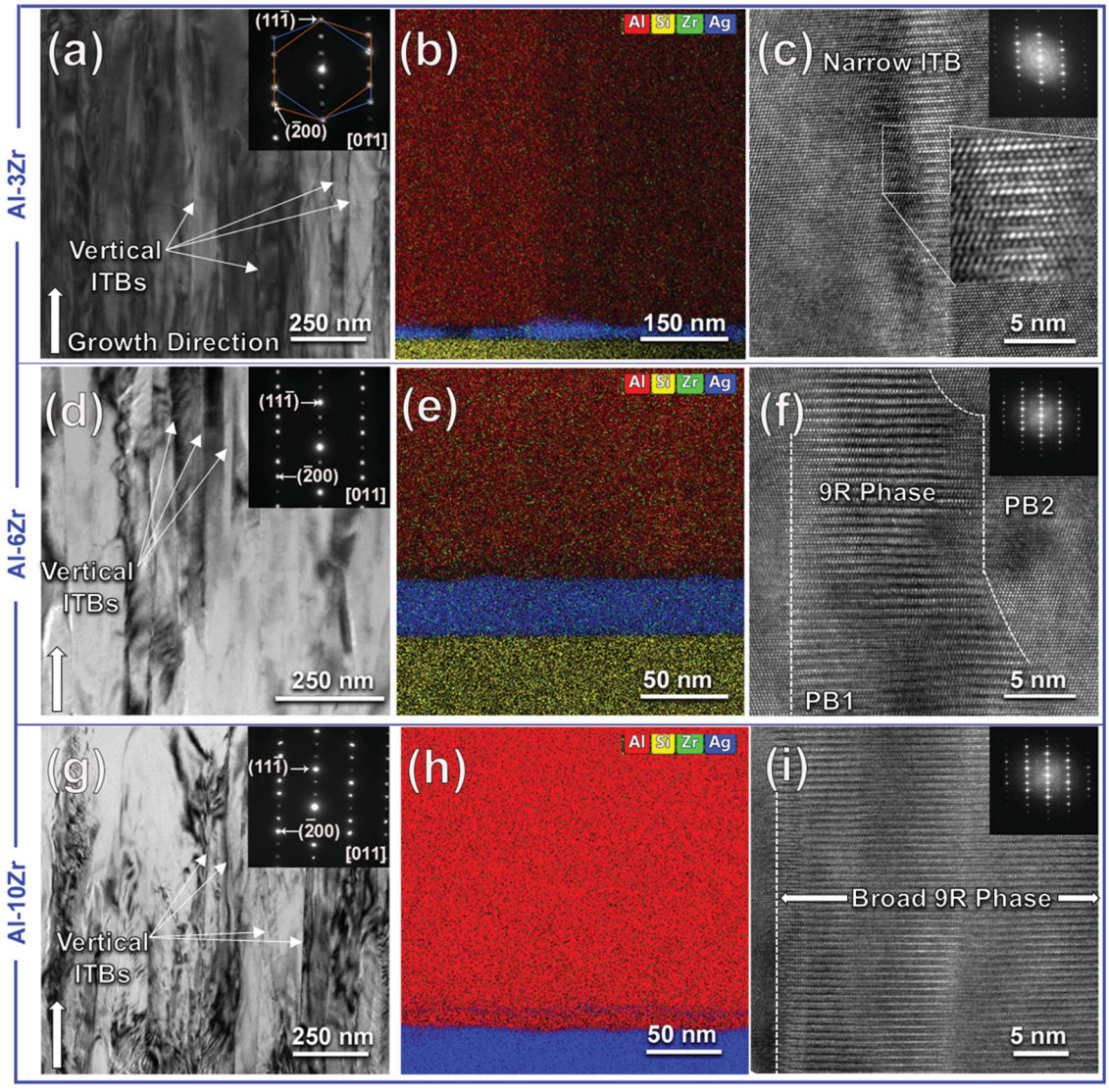

Figure 3. Cross-section TEM (XTEM) micrographs of NT Al-Zr alloy films. (a,d,g) Bright-field (BF) XTEM image with inserted SAD pattern showing columnar grains bounded by ITBs. Columnar refinement occurs at higher Zr content. (b,e,h) EDS maps showing complete solid solution at all compositions. (c,f,h) High-resolution TEM (HRTEM) images of (c) narrow ITB, (f) extended ITB, forming 9R phase, and (i) broad 9R phase, spanning ~40 nm.

9R phase forms [38]. It has been suggested that the shear stress present at the edge of island nuclei during island film growth drives the migration of the b_1 partial, forming 9R [25]. However, detwinning is normally expected to occur as the high SFE retracts the partial dislocations bounding the faults. MD simulations conducted by Li et al. have shown that 9R phase in pure Al is unstable, whereas the addition of Fe solute stabilizes the twin structure [30]. The addition of Zr solute may alter the energetic landscape during deposition, and as a result, influences both the atomic migrations and detwinning process.

Therefore, density functional theory (DFT) calculations were carried out to assess the impact of Zr solute on the SFE and the migration energy of atomic surface clusters. A schematic depicting the methodology for the calculations is shown in Fig. S4. The results in Figure 4(c) show an addition of ~5 at.% Zr drops the SFE from ~125 to 108 mJ/m^2. Figure 4(d,e) indicates that the energy barrier for the migration of a surface trimer increases substantially from 0.101 to 0.146 eV and increases from 0.098 to 0.119 eV for a surface heptamer. Both results support the formation of ITBs and help explain the high degree of stabilization of 9R phase as shown in Figure 4(b). The increasing energy barriers for surface cluster migration suggest Zr prevents detwinning, leading to the stabilization of the partial dislocations that form 9R phase. In addition, further DFT calculations indicate that Zr prefers to reside at substitutional sites (lower formation energy, −1.22 eV, compared to +2.62 eV for an octahedral site), which could prevent

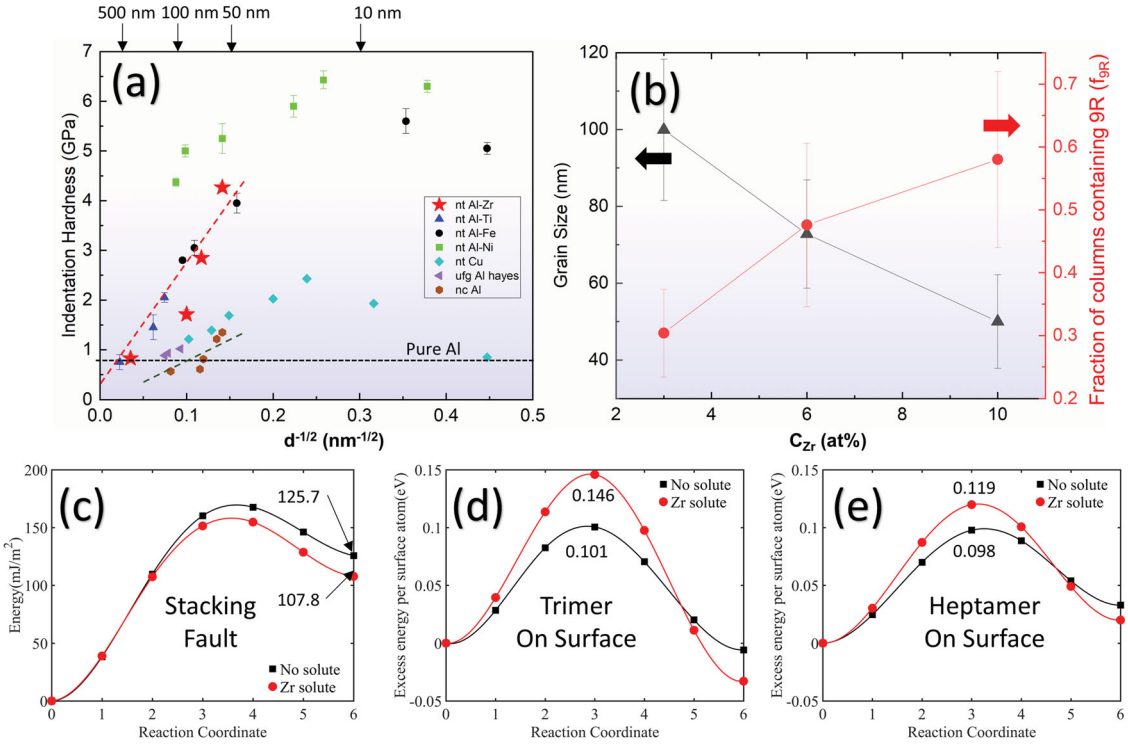

Figure 4. (a) Hall-Petch plot comparing hardness of NT Al-Zr with Al and other NT Al-X systems and NT Cu [9,13,30–32,39] (b) Fraction of columns containing 9R phase and grain size evolution with at% Zr. (c) DFT calculation comparing energy required for stacking fault formation in pure Al and Al-Zr. Zr reduces the stable stacking fault energy of Al. (d–e) DFT calculation showing excess energy per surface atom for (d) trimer and (e) heptamer clusters to move from an FCC stacking position to a faulted position. Zr increases the energy barrier for surface migration.

self diffusion of Al atoms during growth, leading to a higher density of twins and SFs retained in the film. Consequently, the nucleation of 9R phase is promoted by the traction stress (during island coalescence) and the high energy barrier for surface migration of atomic clusters and a reduced defect formation energy induced by Zr solutes facilitate stabilization of the 9R phase in Al-Zr alloys.

The high strengths of these NT Al-Zr alloy films arise from several factors that are closely tied to the unique microstructure of the films. These include solid solution strengthening (SSS), ITB induced boundary strengthening, and 9R phase induced strengthening. First, although the equilibrium solid solubility of Zr in Al is minimal, due to the high quenching rate in sputtering, a high concentration of Zr atoms can be trapped in the matrix, forming a supersaturated solid solution. The Zr solute atoms induce lattice distortion and the consequent SSS in NT Al-Zr can be estimated by using the Fleischer equation [40],

$$\Delta\sigma_{SS} = 0.0235 * G_{solv} * {\varepsilon_s}^{3/2} c^{1/2} \qquad (1)$$

where $\Delta\sigma_{ss}$ represents the strength increment, G_{solv} is the shear modulus of Al, c is the solute concentration. ε_s is defined as:

$$\varepsilon_s = \left| \frac{\frac{1}{G_{solv}} * \frac{dG}{dc}}{1 + \frac{1}{2}\left|\frac{1}{G_{solv}} * \frac{dG}{dc}\right|} - 3 * \frac{1}{a_{solv}} * \frac{da}{dc} \right| \qquad (2)$$

where G is the shear modulus of the alloy, a_{solv} and a are the lattice parameter of Al and the alloy, respectively. α is taken to be 0.0235, a material dependent factor calculated for Ni-W alloys, that was determined to be suitable for these solid solution nt Al alloys [31,35]. For this calculation, it is assumed that both dG/dc and da/dc are linear with solute concentration. These calculations demonstrate the minor hardening contribution from SSS, with only a $\Delta\sigma_{ss}$ increase of 0.0283 GPa for 10at% Zr, after considering the Tabor (2.7) [41] and Taylor (3.1) factors [42]. This calculation suggests that SSS alone cannot account for the high strength of the NT Al-Zr alloys.

The Hall-Petch plot in Figure 4(a) captures the impact of the TB induced strengthening effects. Since the influence of SSS is minor, the large increase in Hall-Petch slope (k_y) to $\sim$9.29 GPa$*$nm$^{1/2}$ (comparing with 4.7 GPa$*$nm$^{1/2}$ NC Al) can be attributed to the presence of both sharp ITBs and expanded 9R phase, analogousto thin and thick GBs reported recently in Ni alloys [43].

Ding et al. [43] show that a thick GB leads to a higher Hall-Petch slope compared with the same alloys with thin GBs. MD simulations prove that the thick GB is more effective at strengthening polycrystalline materials [43]. The ability of ITBs to provide strengthening by blocking dislocations has been clearly supported by both in-situ nanoindentation and MD simulations, demonstrating the ability of ITBs in Al films to resist dislocation pile-ups and induce substantial work hardening [22]. In addition, MD simulations of compression tests of NT Al–Fe further elucidate the extensive interactions between dislocations and 9R phase [30]. The high fraction of 9R phase in these NT Al-Zr alloys provides an opportunity to isolate 9R's impact on Hall-Petch strengthening. The presence of the 9R phase (Figure 3(f)) and the periodic SF structure means that mobile dislocations will be obstructed by 9R phase, or diffuse ITBs, in addition to the narrow (sharp) ITB columnar boundaries. 9R phases effectively block the transmission of mobile dislocations, and adds a new component to the strengthening equation as follows:

$$\sigma = \sigma_0 + \Delta\sigma_{ss} + k_{ITB}d^{-1/2} + k_{9R}L^{-1/2} \quad (3)$$

where k_{9R} and L represent the 9R strengthening coefficient and spacing between 9R regions, respectively. Since MD simulations have demonstrated the similarity between ITBs and high angle GBs in preventing dislocation emission [44,45], a k value of $\sim$4.7 GPanm$^{1/2}$ [9] for NC Al (Figure 4(a)) was adopted for k_{ITB}, and d represents the columnar grain size measured in this study. L represents the spacing between regions of 9R phase, and was determined based on a ratio between the average 9R width (d_{9R}) and the fraction of columns containing 9R phase (f_{9R}), plotted in Figure 4(b). Fig. S5 illustrates the terms described here schematically and relates them to the microstructure. The equation for L is given by:

$$L = \frac{d_{9R}}{f_{9R}} - d_{9R} \quad (4)$$

With L determined, Equation (3) was used to estimate k_{9R}, which was calculated to be 6.9 GPanm$^{1/2}$. It is reasonable that k_{9R} is greater than k_{ITB} (4.7 GPanm$^{1/2}$) as the diffuse ITB and periodic SF structure provide additional obstacles to dislocation motion, as supported by MD simulations [30]. This simple estimation demonstrates the substantial impact of 9R phase on the mechanical properties of these NT Al alloys.

Conclusions

Sputtered Al-Zr alloys have a fine columnar structure composed of ITBs and abundant 9R phase. The addition of Zr leads to the formation of supersaturated solid solution alloys. These microstructural features, coupled with the high solid solubility, lead to outstanding mechanical strengths (a high hardness reaching 4.2 GPa). DFT calculations reveal that the addition of Zr reduces the SFE of the Al alloy, and the detwinning energy barrier has been increased substantially, attributing to the formation of high twin density and broad 9R phase. Analyses show that ITBs as well as 9R phase play a critical role in the strengthening of NT Al alloys.

Acknowledgements

This project is primarily funded by DoE-BES (Basic Energy Sciences) under grant number DE-SC0016337. The ASTAR crystal orientation system in TEM microscope is supported by ONR-DURIP award N00014-17-1-2921. Access to the Microscopy Facilities at Purdue University and Center for Integrated Nanotechnologies (managed by Los Alamos National Laboratory) are also acknowledged. Atomistic simulations were completed utilizing the Holland Computing Center of the University of Nebraska, which receives support from the Nebraska Research Initiative.

Disclosure statement

No potential conflict of interest was reported by the author(s).

Funding

This project is primarily funded by DoE-BES (Basic Energy Sciences) [grant number DE-SC0016337]. The ASTAR crystal orientation system in TEM microscope is supported by ONR-DURIP award N00014-20-1-2659.

ORCID

N. A. Richter http://orcid.org/0000-0003-3273-2276
Y. F. Zhang http://orcid.org/0000-0002-5544-7534
R. Su http://orcid.org/0000-0003-1183-3641
Q. Li http://orcid.org/0000-0001-5442-259X
S. Xue http://orcid.org/0000-0002-8445-8718
J. Wang http://orcid.org/0000-0001-5130-300X
H. Wang http://orcid.org/0000-0002-7397-1209
X. Zhang http://orcid.org/0000-0002-8380-8667

References

[1] Shin J, Kim T, Kim DE, et al. Castability and mechanical properties of new 7xxx aluminum alloys for automotive chassis/body applications. J Alloys Compd. 2017;698:577–590.
[2] Liddicoat PV, Liao XZ, Zhao Y, et al. Nanostructural hierarchy increases the strength of aluminium alloys. Nat Comm. 2010;1(6):1–7.
[3] Ma K, Wen H, Hu T, et al. Mechanical behavior and strengthening mechanisms in ultrafine grain precipita tion-strengthened aluminum alloy. Acta Mater. 2014;62(1):141–155.
[4] Hall EO. The deformation and ageing of mild steel: III discussion and results. Proc Phys Soc Sect B. 1951;64(9):747–753.

[5] Petch NJ. The cleavage strength of polycrystals. J Iron Steel Inst. 1953;174:25–28.
[6] Fleischer RLL. Substitutional solution hardening. Acta Metall. 1963;11:203–209.
[7] Yen Ø, Sjölander E, Sjölander S, et al. Strengthening mechanisms in solid solution aluminum alloys. Metall Mater Trans A. 2006;37A:1999–2006.
[8] Jobba M, Mishra RK, Niewczas M. Flow stress and work-hardening behaviour of Al-Mg binary alloys. Int J Plast. 2015;65:43–60.
[9] Kamikawa N, Hirochi T, Furuhara T. Strengthening mechanisms in ultrafine-grained and sub-grained high-purity aluminum. Metall Mater Trans A. 2019;50(1):234–248.
[10] Esquivel J, Wachowiak MG, O'Brien SP, et al. Thermal stability of nanocrystalline Al-5at.%Ni and Al-5at.%V alloys produced by high-energy ball milling. J Alloys Compd. 2018;744:651–657.
[11] Beyerlein IJ, Zhang X, Misra A. Growth twins and deformation twins in metals. Annu Rev Mater Res. 2014;44(1):329–363.
[12] Lu L, Shen Y, Chen X, et al. Ultrahigh strength and high electrical conductivity in copper. Science. 2004;304(5669):422–426.
[13] Lu L, Chen X, Huang X, et al. Revealing the maximum strength in nanotwinned copper. Science. 2009;323(5914):607–610.
[14] Anderoglu O, Misra A, Wang H, et al. Epitaxial nanotwinned Cu films with high strength and high conductivity. Appl Phys Lett. 2008;93(8):5–8.
[15] Bufford D, Wang H, Zhang X. High strength, epitaxial nanotwinned Ag films. Acta Mater. 2011;59(1):93–101.
[16] Zhang X, Misra A, Wang H, et al. Enhanced hardening in Cu/330 stainless steel multilayers by nanoscale twinning. Acta Mater. 2004;52(4):995–1002.
[17] Zhang X, Misra A, Wang H, et al. Strengthening mechanisms in nanostructured copper/304 stainless steel multilayers. J Mater Res. 2003;18(7):1600–1606.
[18] Anderoglu O, Misra A, Wang J, et al. Plastic flow stability of nanotwinned Cu foils. Int J Plast. 2010;26(6):875–886.
[19] Jin ZH, Gumbsch P, Albee K, et al. Interactions between non-screw lattice dislocations and coherent twin boundaries in face-centered cubic metals. Acta Mater. 2008;56(5):1126–1135.
[20] Wang YM, Sansoz F, LaGrange T, et al. Defective twin boundaries in nanotwinned metals. Nat Mater. 2013;12(8):697–702.
[21] Liu Y, Jian J, Chen Y, et al. Plasticity and ultra-low stress induced twin boundary migration in nanotwinned Cu by in situ nanoindentation studies. Appl Phys Lett. 2014;104(23):231910.
[22] Bufford D, Liu Y, Wang J, et al. In situ nanoindentation study on plasticity and work hardening in aluminium with incoherent twin boundaries. Nat Commun. 2014;5:1–8.
[23] Lee JH, Holland TB, Mukherjee AK, et al. Direct observation of Lomer-Cottrell locks during strain hardening in nanocrystalline nickel by in situ TEM. Sci Rep. 2013;3:1061.
[24] Schulthess TC, Turchi PEA, Gonis A. Systematic study of stacking fault energies of random Al-based alloys. Acta Mater. 1998;46(6):2215–2221.
[25] Bufford D, Liu Y, Zhu Y, et al. Formation mechanisms of high-density growth twins in aluminum with high stacking-fault energy. Mater Res Lett. 2013;1(1):51–60.
[26] Zhang X, Bufford D, Wang H, et al. Method for producing high stacking fault energy (SFE) metal films, foils, and coatings with high-density nanoscale twin boundaries. 2018. 10023977 B2.
[27] Yu KY, Bufford D, Chen Y, et al. Basic criteria for formation of growth twins in high stacking fault energy metals. Appl Phys Lett. 2013;103(18):181903.
[28] Xue S, Fan Z, Chen Y, et al. The formation mechanisms of growth twins in polycrystalline Al with high stacking fault energy. Acta Mater. 2015;101:62–70.
[29] Xue S, Kuo W, Li Q, et al. Texture-directed twin formation propensity in Al with high stacking fault energy. Acta Mater. 2018;144:226–234.
[30] Li Q, Xue S, Wang J, et al. High-strength nanotwinned Al alloys with 9R phase. Adv Mater. 2018;30(11):1–9.
[31] Zhang YF, Xue S, Li Q, et al. Microstructure and mechanical behavior of nanotwinned AlTi alloys with 9R phase. Scr Mater. 2018;148:5–9.
[32] Zhang YF, Li Q, Xue S, et al. Ultra-strong nanotwinned Al–Ni solid solution alloys with significant plasticity. Nanoscale. 2018;10:22025–22034.
[33] Xue S, Li Q, Xie DY, et al. High strength, deformable nanotwinned Al–Co alloys. Mater Res Lett. 2019;7(1):33–39.
[34] Zhang YF, Li Q, Gong M, et al. Deformation behavior and phase transformation of nanotwinned Al/Ti multilayers. App Surf Sci. 2020;527:146776.
[35] Li Q, Xie D, Shang Z, et al. Coupled solute effects enable anomalous high-temperature strength and stability in nanotwinned Al alloys. Acta Mater. 2020;200:378–388.
[36] Zhang Y, Su R, Xie D, et al. Design of super-strong and thermally stable nanotwinned Al alloys via solute synergy. Nanoscale;12(39). 2020.
[37] Wang J, Anderoglu O, Hirth JP, et al. Dislocation structures of $\sigma 3$ 112 twin boundaries in face centered cubic metals. Appl Phys Lett. 2009;95(2):93–96.
[38] Wang J, Li N, Anderoglu O, et al. Detwinning mechanisms for growth twins in face-centered cubic metals. Acta Mater. 2010;58(6):2262–2270.
[39] Hayes RW, Witkin D, Zhou F, et al. Deformation and activation volumes of cryomilled ultrafine-grained aluminum. Acta Mater. 2004;52(14):4259–4271.
[40] Rupert TJ, Trenkle JC, Schuh CA. Enhanced solid solution effects on the strength of nanocrystalline alloys. Acta Mater. 2011;59(4):1619–1631.
[41] Misra A, Hirth JP, Hoagland RG. Length-scale-dependent deformation mechanisms in incoherent metallic multilayered composites. Acta Mater. 2005;53(18):4817–4824.
[42] Mata M, Anglada M, Alcalá J. Contact deformation regimes around sharp indentations and the concept of the characteristic strain. J Mater Res. 2002;17(5):964–976.
[43] Ding J, Neffati D, Li Q, et al. Thick grain boundary induced strengthening in nanocrystalline Ni alloy. Nanoscale. 2019;11(48):23449–23458.
[44] Zhang X, Misra A, Wang H, et al. Nanoscale-twinning-induced strengthening in austenitic stainless steel thin films. Appl Phys Lett. 2004;84(7):1096–1098.
[45] Gu P, Kad BK, Dao M. A modified model for deformation via partial dislocations and stacking faults at the nanoscale. Scrip Mater. 2010;62(6):361–364.